Landslides (2018) 15:593–612
DOI 10.1007/s10346-017-0922-8
Received: 13 July 2017
Accepted: 10 November 2017
Published online: 21 November 2017

Sheng Hu · Haijun Qiu · Xingang Wang · Yu Gao · Ninglian Wang · Jiang Wu · Dongdong Yang · Mingming Cao

Acquiring high-resolution topography and performing spatial analysis of loess landslides by using low-cost UAVs

Abstract The Loess Plateau is a region in China prone to frequent geological disasters, where thousands of loess landslides can be found. Conventional field survey methods are inadequate for the requirements of fine spatial analysis of landslides. Due to its numerous advantages (fast, efficient, low cost, safe, and able to acquire high-resolution data), structure from motion (SfM) technique to photogrammetric orientation of flights and modeling applied to photographs taken by unmanned aerial vehicles (UAVs) equipped with a camera has become a powerful new tool for the generation of high-resolution topography that has emerged in recent years, which has become a powerful new technique for acquiring high-resolution topographic data. In this study, we conducted nearly two months of field UAV surveys of loess landslides on the Loess Plateau, eventually established 3D digital models for 11 loess landslides, and produced high-resolution digital orthophoto maps (DOMs) and digital elevation models (DEMs). High-resolution spatial analysis of the loess landslides (mainly including characteristic parameter extraction, topography profile analysis, surface feature analysis, and hydrologic analysis) was performed using Agisoft PhotoScan, ArcGIS 10.2, Global Mapper 17, and Origin Pro 9.0. The UAV technique allows us to further understand the micro-level internal spatial and structural characteristics of loess landslides. Moreover, not only does it allow us to accurately measure the characteristic geometric parameters but also enables us to detect the surface details of loess landslides (e.g., textures, fissures, and micro-landforms). Manifestly, we can also deduce the original structural characteristics and possible inducement mechanism of landslides based on a combination of high-resolution data acquired by UAVs, proper ground surveys, and theoretical knowledge. In summary, the low-cost UAVs are highly and especially suitable for surveys and digital terrain analysis of landslides on the Loess Plateau with sparse vegetation.

Keywords Structure from motion · UAVs · High-resolution · Loess landslide · Spatial analysis · Loess Plateau

Introduction

Loess, a type of porous, weakly cemented, loose sediment with a specific mineral composition, form, and properties, covers approximately 10% of the world's land area. Quaternary loess is widely distributed in numerous countries and regions of the world where it is closely related either to desert or Gobi, e.g., the loess in China, or to continental glaciation, e.g., the loess in Central Europe and North America (Flint 1947; Liu and Chang 1962; Smalley 1971; Liu 1985; Derbyshire and Mellors 1988). In China, loess covers an area of approximately 6.31×10^5 km^2, accounting for about 6.6% of the country's total land area, and is mainly distributed on the Loess Plateau (Liu 1985; Qiu et al. 2016). Liu (1985) considered that the Cenozoic and Mesozoic detrital sediments that form the deserts and Gobi northwest of the loess area are probably the source material of the loess accumulation in China.

Since the Quaternary, loess has been continuously deposited on the Loess Plateau with intermittent rising of crust, resulting in an increase in its thickness. In addition, as a result of erosion by rainfall and fluvial erosion, a multitude of loess slopes have only maintained a critical balance state (Chen et al. 2013). With the intensification of human economic and engineering activities in recent years (e.g., mining, roadwork, slope excavation, agricultural irrigation, and urban expansion), this state can be easily disrupted. As a result, loess landslides are occurring at a significantly increasing frequency, posing a serious threat to people's lives and property. The landslide at the Baqiao Brickyard in Xi'an City (Zhuang and Peng 2014) and the landslide in Gaolou Village, Huaxian County (Zhang et al. 2009) are two representative catastrophic landslides that have occurred. The latest geological disaster survey data show thousands of loess landslide hazards and potential hazard locations in the Shaanxi section of the Loess Plateau alone (Qiu et al. 2017; Zhuang et al. 2017). Conventional field surveys require tremendous human labor, material, and financial resources, and the acquired characteristic parameters of loess landslides are only at the macroscopic level and not sufficiently accurate. Some landslides pose a great threat to surveyors' personal safety. Therefore, using a low-cost, efficient, safe, and time- and effort-saving survey technique to acquire high-resolution topographic data and images of landslides is of great importance to an accurate understanding of the topographic, surface, and structural characteristics of loess landslides.

In fact, the geospatial-scale problem has always been an obstacle preventing us from accurately understanding geographical phenomena or processes. Remote sensing technology has played a pivotal role in large-scale geographical disaster surveys and monitoring in recent decades (Niethammer et al. 2012; Casagli et al. 2016; Shafique et al. 2016). With the advancement of observation methods and technologies, some new measuring techniques have been used in landslide surveys worldwide, such as remote sensing on landslides (Metternicht et al. 2005; Tofani et al. 2014; Sun et al. 2017; Yang et al. 2017), interferometric synthetic aperture radar (InSAR) (Sun et al. 2015; Bayer et al. 2017), airborne and terrestrial geodetic light detection and ranging (LIDAR) scans (Tarolli 2014), terrestrial three-dimensional (3D) laser scans (Niethammer et al. 2012; Razak et al. 2013), and Quad-rotor UAVs or fixed wing aircraft photogrammetry (Niethammer et al. 2012; Dąbski et al. 2017). In particular, the latter three methods can acquire centimeter-scale high-resolution digital terrain models (DTMs) from point clouds (Carter et al. 2007). Anyway, multitemporal analysis plays a vital role in the dynamic process of landslides monitoring all the time (Ventisette et al. 2014). However, although the aforementioned methods are suitable for large-scale field surveys and have very high measurement accuracy, they are all

significantly limited by their high cost and lack of flexibility and convenience. For surveys of slope-scale landslides, conventional aerial or satellite imagery has relatively low resolution from which the textural features (e.g., fissure structure and small displacements) of landslides cannot be clearly identified. This type of feature information is, however, of crucial importance to the understanding of the dynamic processes of landslides (Niethammer et al. 2012). The ability of imagery to manifest loess landslides varies significantly with its resolution (Fig. 1). Recently, the unmanned aerial vehicle (UAV) photogrammetric technique has become a new tool for generating high-resolution topography (Niethammer et al. 2012; Dąbski et al. 2017; Kršák et al. 2016; Turner et al. 2016; Watanabe and Kawahara 2016; Cook 2017; Pineux et al. 2017). This technique has opened the gate to the acquisition of high-quality field data (Pineux et al. 2017). However, depending on the aerial measurement accuracy and model, UAVs can cost a few hundred to tens of thousands of US dollars. Small quadrotor UAVs that cost a few hundred US dollars (e.g., DJI Phantom series, DJI Mavic Pro, and DJI Inspire series) are a favorable choice for preliminary field surveys on landslides due to their low cost, flexibility, and portability and are in no way inferior to professional UAVs in terms of acquiring high-resolution topographic data and images of landslides (Niethammer et al. 2012; Kršák et al. 2016).

Previous researchers have achieved fruitful works on loess landslide research. Their researches are primarily focused on the following areas: (a) the distribution, characteristics, and power-law correlations of loess landslides (Qiu et al. 2013; Zhuang and Peng 2014); (b) the effects of topography on loess landslides (Qiu et al. 2016; Qiu et al. 2017); (c) the formation mechanism of loess landslides (Tu et al. 2009; Peng et al. 2015; Shi et al. 2016; Leng et al. 2017); and (d) experimental simulations of loess landslides (Tu et al. 2009; Cui et al. 2017; Zhang et al. 2017). However, most of the aforementioned researches were based on macroscopic field surveys. Currently, a considerable lack of high-resolution field surveys in loess landslides and relevant researches are rarely reported. Hence, the present study is performed with two main objectives. One objective is to use low-cost and consumer-level UAVs (DJI Phantom 3 (4k)) to conduct

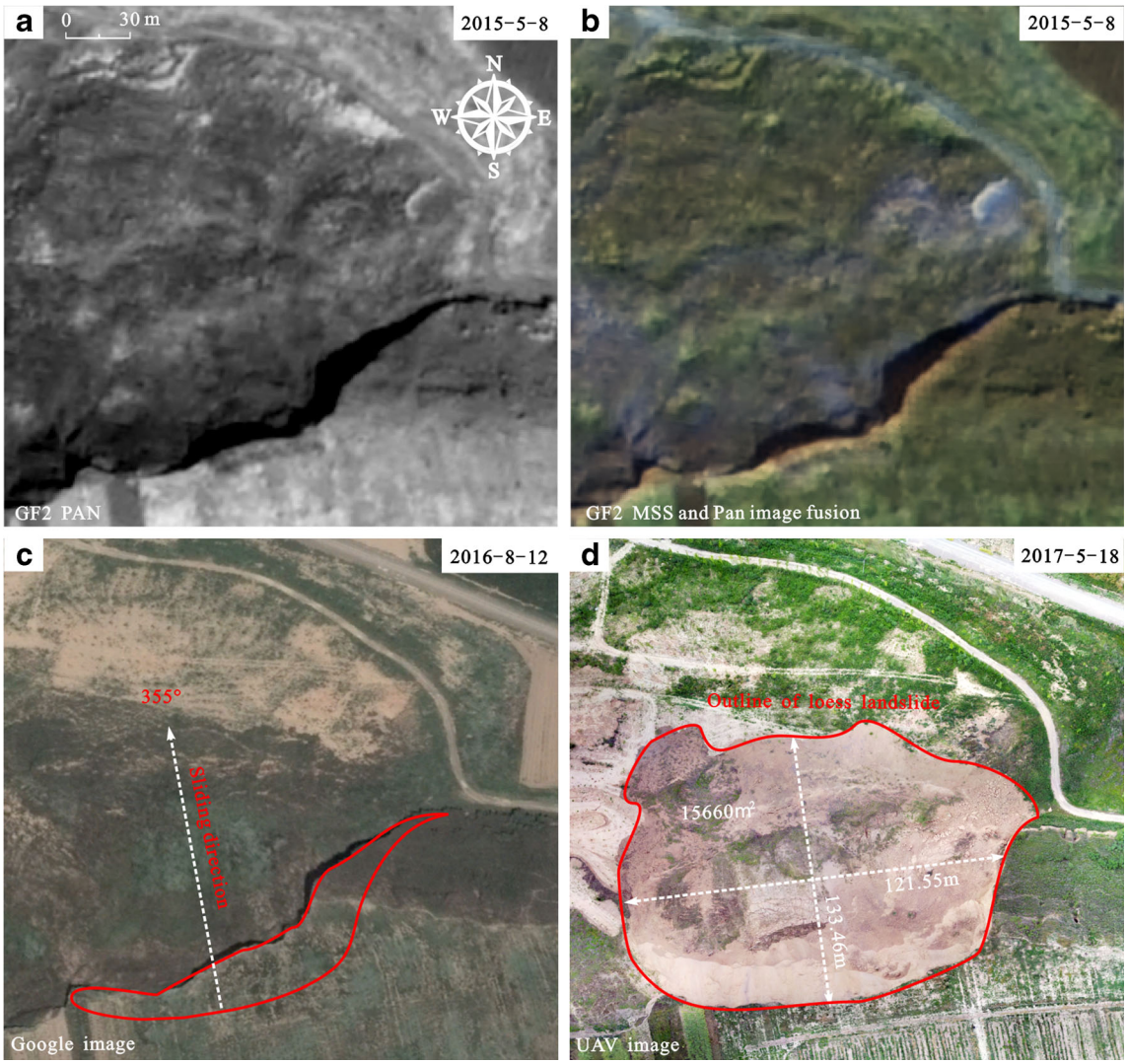

Fig. 1 Ability of different resolution images to show the L06 landslide in the South Jingyang Tableland. **a** GF2 PAN 0.70 m. **b** GF2 MSS and Pan image fusion 0.70 m. **c** Google image 0.54 m. **d** UAV image 0.03 m. **c** was photographed by Google satellite before sliding on August 12, 2016. **d** was photographed by UAVs within a week after sliding on May 18, 2017

landslide surveys on the Loess Plateau and rapidly acquire high-resolution DEMs and DOMs of landslides in the Loess Hilly area and the Loess Tableland area, allowing 3D digital models for loess landslides to be established. The other objective is to implement and improve the loess landslides mapping in detail, enabling spatial analysis of typical loess landslides to be performed to better reveal their spatial distribution characteristics, structures, and hydrological paths.

Study area

China has the most extensive and representative distribution of loess in the world. Thick, continuous loess layers cover the middle reaches of the Yellow River Basin, forming the magnificent Loess Plateau. Because the loess layers are thick but structurally loose, have high porosity with developed columnar joints, and are prone to erosion and stripping, the Loess Plateau is plagued by the most severe soil erosion problem in China and prone to frequent geological disasters (e.g., loess landslides, collapses, and mudslides) (Liu 1985; Chen et al. 2013; Peng et al. 2015; Qiu et al. 2017; Zhuang et al. 2017). The Loess Plateau is characterized by sparse vegetation, large areas of bare rock and soil, and a tendency toward frequent landslides (Peng et al. 2017a, b). The Loess Hilly area and the Loess Tableland area are the two main geomorphic units of the Loess Plateau, where geological loess disasters mainly occur (Lei 2017). Therefore, we conducted field UAV surveys on landslides in these areas (Fig. 2). Of the landslides surveyed in this work, five were located in the Loess Hilly area in northern Shaanxi (specifically, Zhidan County in Yan'an City and Jingbian County in Yulin City) and six in the Loess Tableland area in the Guanzhong Basin (specifically, Baqiao District in Xi'an City and Jingyang County in Xianyang City). Most of them were homogeneous loess landslides induced by rainfall, engineering excavation, and agricultural irrigation. In addition, some were old landslides that had occurred several years ago, and some were new landslides that occurred one to two months preceding the surveys.

Material and methods

Data acquisition and processing

Preliminary test of UAV accuracy

The DJI Phantom 3 (4k) UAV manufactured by Da-Jiang Innovations Science and Technology Co., Ltd. (trading as DJI) with a unit cost of production of approximately US$588 was used in this work. The main technical parameters of the DJI Phantom 3 (4k) UAV are as follows: weight, 1280 g; hovering precision, ± 0.5 m (vertical) and ± 1.5 m (horizontal); maximum flight speed, 16 m/s; operating temperature, 0–40 °C; flight time, approximately 25 min; lens, 94° (field of view) and 20 mm (35-mm format equivalent) f/2.8; and maximum image resolution, 4000 × 3000.

Surveying and mapping accuracy and resolution have always been of concern for small UAVs. Cook (2017) constructed a 3D topographic map of the Daan River Gorge in western Taiwan using DJI Phantom 2 UAVs, and concluded that UAVs could generate data suitable for measuring topographic changes at the scale of a channel reach. Pineux et al. (2017) quantified diffuse

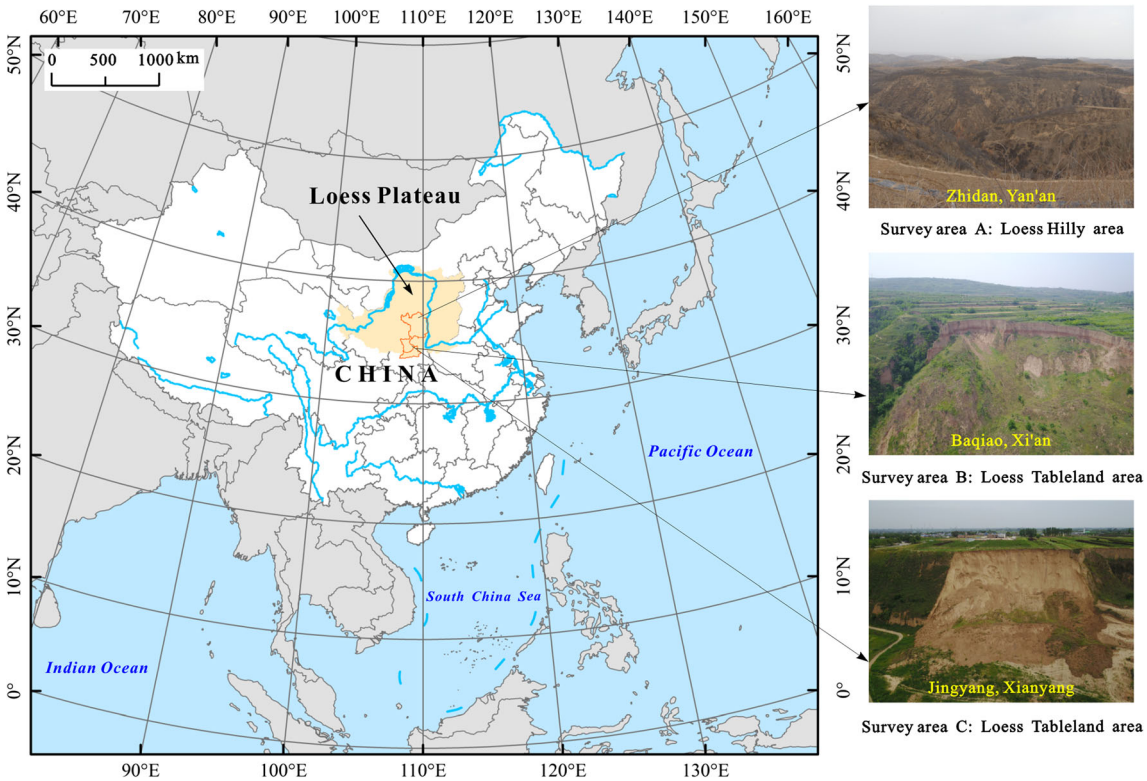

Fig. 2 Location of the Loess Plateau and the UAV survey areas: Loess Hilly area and Loess Tableland area

erosion in an agricultural watershed using Gatewing X100 UAVs and achieved relatively satisfactory results. Our original objective is to gradually establish high-resolution topographic models and orthoimage databases for dozens of loess landslides to conduct high-resolution topographic analysis of loess landslides. Undoubtedly speaking, ground control points (GCPs) are essential for accurate aerial photogrammetric surveys (Lucieer et al. 2014; James et al. 2017; Pineux et al. 2017). However, landslide monitoring was not a task for the present stage of this research, so GCPs were not used in our UAV surveys. But UAV and SfM techniques play a more important role in landslide monitoring seen from predecessors' outstanding works (Niethammer et al. 2012; Al-Rawabdeh et al. 2016; Daakir et al. 2015; Peterman 2015; Turner et al. 2016; Fernández et al. 2016), as well as analysis of accuracy of the DEMs and DOMs (Niethammer et al. 2012; Fernández et al. 2016; Hsieh et al. 2016; Lindner et al. 2016). It is comforting to know that, with the development of navigation technology, some advanced technologies such as high-price and high-precision GNSS and Inertial Navigation System are equipped to drones, which can avoid placing GCPs and significantly improve work efficiency (Carrillo et al. 2012; Eure et al. 2013; Lindner et al. 2016). Previous research results have demonstrated that 3D landslide models generated by using UAV and SfM techniques have very high relative accuracy and, to a certain extent, can meet the requirements for preliminary field surveys of landslides (Dąbski et al. 2017; Gruszczyński et al. 2017; James et al. 2017). Nonetheless, we still would like to determine the relative accuracy of high-resolution DOMs and DEMs generated by DJI UAVs without GCPs. Thus, prior to completing the field surveys of landslides, we used a UAV to construct 3D images of some runoff plots on our campus and preliminarily examined the repeat error of the DOMs and DEMs generated by the UAV in the horizontal and vertical directions. We measured the DOMs and DEMs using ArcGIS 10.2 and Global Mapper 17 and found that the measurements were nearly consistent with the actual lengths, widths, heights, and gradients (Fig. 3). Figure 4 shows the controlled locations of the UAV and the angles of the UAV camera

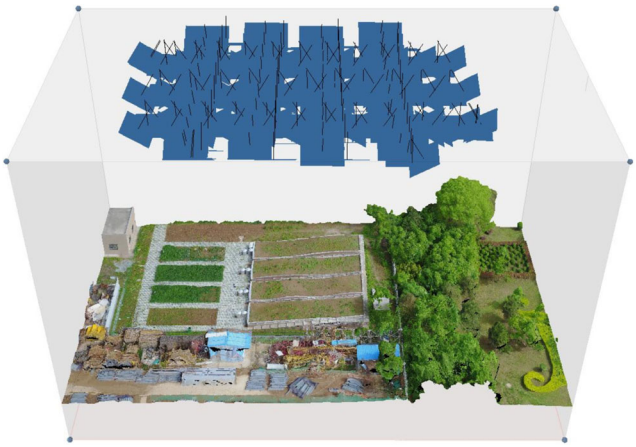

Fig. 4 The positions and angles of the drone's camera in the sky

(capturing 187 images, flying altitude 47 m, overlap and sidelap 75%, tilt angle − 45°, orthographic angle − 90°). To examine the repeat error, two UAV flights were conducted to obtain a high-resolution DOM (1.56 cm/pix) and DEM (3.11 cm/pix). In comparing them, we found some differences between the results obtained from the two flights with respect to the same feature point, but the difference in the horizontal repeat error was only approximately 0.5 m (Fig. 5 and Table 1). In addition, we also examined the vertical repeat error of the high-resolution DEM by comparing the profile lines. Surprisingly, the SfM technique exhibited excellent performance in constructing the 3D topographic model. The comparison of the two flights showed that the two profile lines of the same runoff plot exhibited nearly the same relief and an approximately 0.2-m difference in vertical elevation. However, the two profile lines of each runoff plot were almost perfect in manifesting microtopography ((1) convex-concave, (2) concave-convex, (3) complex, and (4) linear), and the slope shape exhibited by the two profile lines was in complete agreement with actual situation. It is worth mentioning that the two lines almost

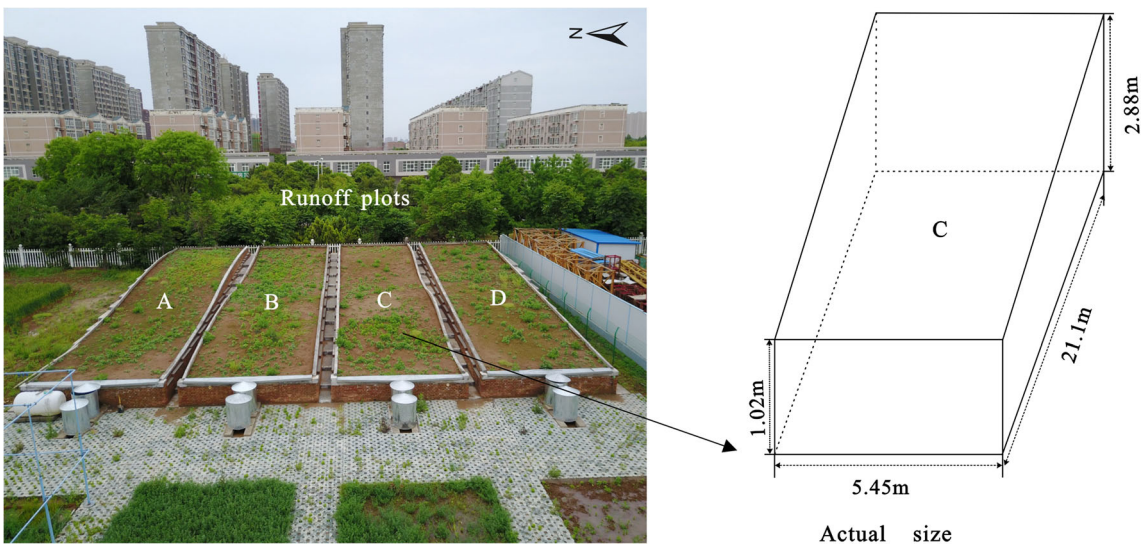

Fig. 3 Different slope patterns of the standard runoff plots on campus

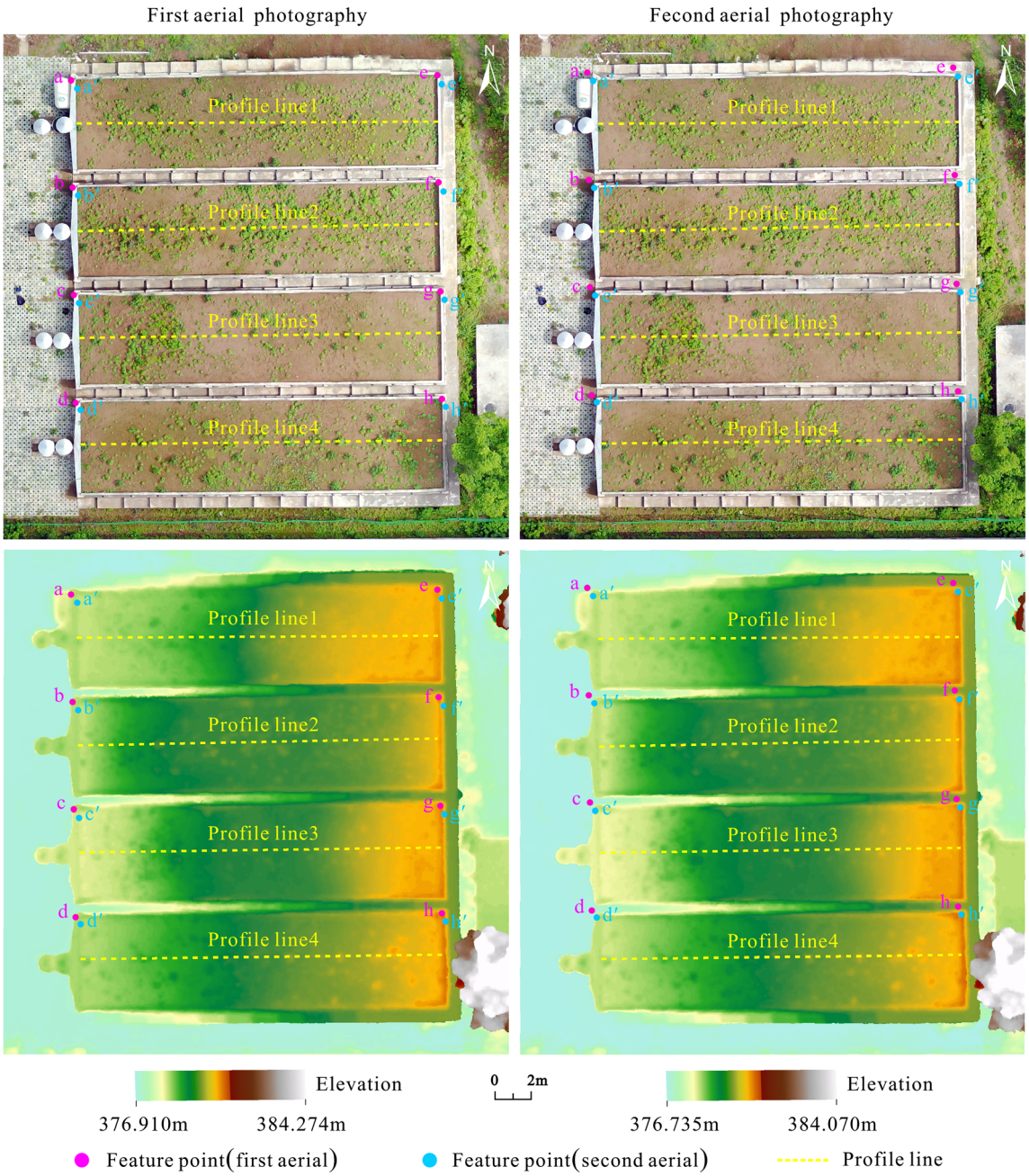

Fig. 5 High-resolution DOM (1.56 cm/pix) and DEM (3.11 cm/pix) of the runoff plots under the two flights

completely overlap under the same height datum. The errors of horizontal and vertical component are not only caused by the uncertainty of measurement in map but have close relationship with systematic error such as GPS positioning of UAV, the platform of camera, and flight vibration. Of course, wind speed is also an important external cause (Fig. 6).

UAV aerial survey

We conducted field surveys of landslides in the Shaanxi section of the Loess Plateau using UAVs for nearly two months (Fig. 7). For one landslide survey, five flight routes from various angles (vertical angle − 90°; tilt angle − 45°) and directions were performed to get the best model and digital product. Flight altitude affects the spatial resolution of the photographs taken by a UAV camera. Therefore, reasonable flight altitudes should be planned based on the peripheral height and topography of a landslide. Experienced operators and a mature operation technique are preconditions for UAV surveys. Flight safety should be the foremost consideration. UAV flights must follow the local laws and regulations. With the popularization and application of consumer-level UAVs, air traffic control departments will supervise and control UAVs with increasing strictness. Ultimately, we completed the UAV photogrammetric mapping of 11 loess landslides (Table 2).

Table 1 Repeated error estimation for the same feature point

Point	x (m)	y (m)	z (m)	Point	x (m)	y (m)	z (m)	RMSE_x	RMSE_y	RMSE_z
a	580,679.888446	3,780,215.450330	378.113	a′	580,680.218998	3,780,214.985390	377.937	0.234	0.329	0.124
b	580,679.970996	3,780,209.491110	378.140	b′	580,680.283437	3,780,209.048730	377.940	0.221	0.313	0.142
c	580,680.037565	3,780,203.550250	378.114	c′	580,680.334502	3,780,203.083690	377.877	0.210	0.330	0.168
d	580,680.150278	3,780,197.561290	378.140	d′	580,680.416424	3,780,197.180610	377.913	0.188	0.269	0.161
e	580,700.157581	3,780,215.716500	379.845	e′	580,700.403419	3,780,215.219280	379.737	0.174	0.352	0.077
f	580,700.240660	3,780,209.773690	379.865	f′	580,700.500042	3,780,209.269480	379.731	0.183	0.357	0.095
g	580,700.338291	3,780,203.735620	379.943	g′	580,700.550326	3,780,203.272240	379.792	0.150	0.328	0.106
h	580,700.422958	3,780,197.779170	379.926	h′	580,700.617795	3,780,197.338290	379.797	0.138	0.312	0.091

Photogrammetric post-processing

Subsequent data processing was performed using Agisoft PhotoScan Professional Edition (Version 1.2.5) (Pineux et al. 2017), a relatively low-cost, practical commercial photogrammetry software program. Sona et al. (2014) found that of the numerous commercial photogrammetry software programs, PhotoScan could produce the best photogrammetric products. Ouédraogo et al. (2014) found that, compared with other photogrammetry software programs, PhotoScan seemed to be not very sensitive to vegetation in images taken by the same camera on the same UAV at the same altitude. The majority of the Loess Plateau is in arid and semiarid regions with sparse vegetation. The vegetation on the landslide masses surveyed in this study was short, and large areas of these landslide masses were bare (Peng et al. 2017a, b). Therefore, extra effort was not required to filter vegetation. The general processing procedure using PhotoScan is as follows: (1) add photos, (2) align photos, (3) build a dense point cloud, (4) build a mesh, (5) build a model texture, (6) build a tiled model, (7) build a DEM, (8) build an orthomosaic, (9) export DEM and DOM. Subsequent spatial analysis of the landslides was performed using ArcGIS 10.2, Global Mapper 17, Coreldraw 12, and Origin Pro 9.0 (Fig. 8).

Spatial analysis of high-resolution landslides

Characteristic parameter extraction

Macroscopic qualitative description or semi-quantitative statistical analysis have been widespread methods to survey landslides in the past (Qiu et al. 2016; Zhuang et al. 2017), whereas there is a significant lack of in-depth quantitative calculation, analysis, and verification. In particular, studies that acquire accurate characteristic parameters and complete spatial analysis of landslides on the Loess Plateau are rarely reported (Su et al. 2017). We extracted and statistically analyzed parameters of the 11 loess landslides using ArcGIS 10.2 and Global Mapper 17 with ease (Table 3). These parameters substantially facilitated the determination of the morphological characteristics, elevation distribution, topographic relief, size, circularity, and sliding direction of loess landslides. As demonstrated in Table 3, the average internal gradient of a single loess landslide ranges from 20.97° to 43.23°, and the average value is 33.21°. Within a 5-m × 5-m analysis window, the minimum and maximum reliefs of a single loess landslide are 1.43 and 6.82 m, respectively, and the average value is 4.87 m. The difference in elevation between the top and the toe of a landslide varies significantly among loess landslides, with the minimum and maximum differences being 26.79 and 114.47 m, respectively. In fact, loess landslides are a type of gravitational landform. The difference in elevation between the front and rear edges of a loess landslide plays a key role in controlling its scale (e.g., length, width, perimeter, and area). As shown in Table 3, positive correlations exist among the length, width, perimeter, and area of a loess landslide.

High-resolution DEMs of landslides can satisfactorily exhibit their micro-level structural characteristics and spatial distribution patterns. Here, a typical loess landslide (Lo6) in the South Jingyang Tableland is used as an example. The percentage frequency distributions of the elevation, aspect, gradient, and relief of the landslide were statistically analyzed (Fig. 9). A phenomenon that rarely occurred in the past but is very interesting can be clearly observed in Fig. 9. For a landslide in the Loess Tableland area, its top is generally flat and has the highest elevation, whereas its

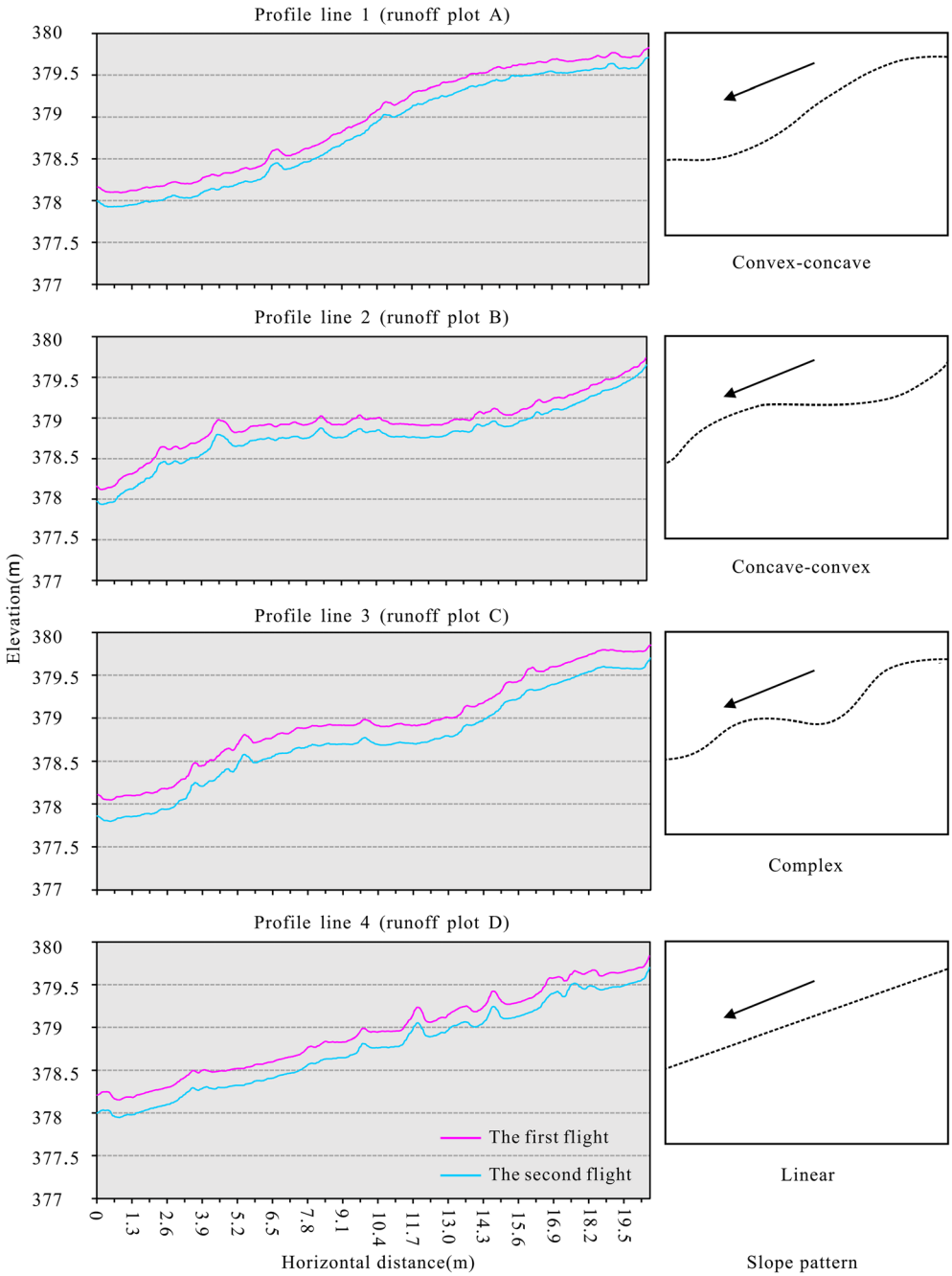

Fig. 6 Profile comparison of the runoff plots under the two flights

main scarp is relatively steep with a plane surface. Figure 9a shows that there is an osculating correspondence between morphology (I-toe, II-main body, III-main scarp, IV-top) and percentage frequency distribution of L06 landslide. Specifically speaking, elevation of the toe (about 15.77% of total frequency) basically changes from low to high (448 to 461 m) with 13-m rangeability, so the corresponding frequency curve has an increasing trend (the maximum frequency is 4.2%). The main body changing from 461 to 480 m occupies the largest proportion (60.05%) of total frequency, and the curve goes up first and then goes down, but far above the average line 1.52% (the maximum approaching 7%). The steep scarp has the highest elevation difference (31 m) and a smaller elevation frequency ratio (15.38%) in the L06 landslide; hence, its curve is basically below the average line (1.52%), presenting a gently downward trend as the elevation ranges from 480 to 511 m. Because the top edge is located in the transition zone of steep main scarp and flat top of landslide, the frequency curve has a sharp turn on 511-m scale. According to different elevation ranges which their frequency curves may reflect different landforms, the external structure of L06 landslide was successfully identified (Fig. 10) to be almost completely the same as that interpreted from the UAV image (Fig. 16).

Fig. 7 Loess landslide field investigation using low-cost UAVs on the Loess Plateau

Figure 9b shows that the high-resolution DEM can clearly exhibit the internal aspect distribution of the Lo6 landslide, which cannot be obtained with conventional survey methods. As a landslide in the Loess Tableland area, its main sliding direction controls its internal aspect distribution. The main sliding direction of the Lo6 landslide is 350°, and its internal aspect is mainly concentrated in NNW-N-NNE direction. There are no counter-slopes and rotational mechanisms in Lo6 landslide (Fig. 9b). Similar to the elevation frequency distribution, the gradient frequency distribution can also be used to determine the topography of a landslide to a certain extent (Fig. 9c). Based on the gradient frequency distribution curve, the flat, gentle slope, steep slope, and escarpment zones of the landslide can be distinguished, but the top and the toe of the landslide in the flat zone cannot be discerned well. Nevertheless, the gradient frequency distribution curve is very sensitive to the main scarp of the landslide—the gradient of the main scarp is very steep (ranging from 57° to 88°), but these steep slopes have a relatively low frequency ratio (8.76% in total). In a 5-m × 5-m analysis window, the variation in the relief frequency distribution curve is basically consistent with the gradient frequency distribution curve—the relief first increases and then decreases. The internal relief of the Lo6 landslide varies between 0 and 22 m, with 0–5 m (accounting for 78%) and especially 1–2 m (accounting for 25.58%) being the dominant ranges (Fig. 9d).

Topography profile analysis

An important topographic survey method is to investigate the cross-section of landslides. By analyzing cross-section, we can further understand the structural characteristics of a landslide (Flageollet et al. 2000; Travelletti and Malet 2012; Watanabe and Kawahara 2016; Zhang et al. 2017). Here, the structural characteristics of two typical loess landslides (L11 and Lo6) from the Loess Hilly area and Loess Tableland area, respectively, are analyzed. The L11 landslide was induced by roadwork (slope cutting), and the Lo6 landslide was induced by rainfall.

The cross-sectional line A–H is set from the top to the toe of the L11 landslide along its main sliding direction (Figs. 11 and 12). As demonstrated in Figs. 11 and 12, the high-resolution DEM has unparalleled advantages over the conventional low-resolution DEM in manifesting the details of the landslide (e.g., fissures, step-type slope, main scarp, and gradient variation). Based on the GIS cross-sectional analysis and the actual stratigraphic survey, the external and internal structural characteristics of the L11 landslide along its main sliding direction can be clearly described. First, from a stratigraphic structural perspective, the bottom layer of the L11 landslide consists of sandstone-mud interbedding, and the top layer is a loess layer overlying the Tertiary red clay greater than 100 m in thickness. From scarp and sliding surface perspective, the L11 landslide which is a typical Loess-Red clay landslide has one main sliding scarp and two secondary scarps related to those sliding surfaces. Second, from a displacement and deformation perspective, the horizontal distance between A and B along the main slope line (A–H) is 12 m, i.e., the landslide has moved over a distance of 12 m horizontally. Based on its sliding conditions, we infer that the L11 landslide had a convex-concave slope shape originally, and over time, its slope has evolved into a concave-convex-concave-convex shape. The sliding plane of the L11 landslide has a generally concave arc shape. Third, from an external structural perspective, the profile line extracted from the high-resolution DEM well reflect its top, main scarp, main body, toe, and even the surface depths of its internal tensile fissures, the shape and angle (58°) of its step-type slope. Fourth, from a difference in elevation and relief perspective, the elevation difference of the L11 landslide is approximately 100 m. In addition, there is also a significant relief difference in different parts of cross-section (AH). The main scarp of the L11 landslide (sub-cross-section AB) is the steepest, with a linear gradient of approximately 71°. Sub-cross-section BC has a linear gradient of approximately 15°. The step-type slope (sub-cross-section CD) has a linear gradient of 45°, with the largest angle being 58°.

Table 2 Landslide locations and flight parameters

Id	Name	Region	Topography	Longitude	Latitude	Photos
L01	Brickyard landslide	Baqiao, Xi'an	Loess Tableland area	109.09° E	34.26° N	525
L02	Baling landslide	Baqiao, Xi'an	Loess Tableland area	109.11° E	34.25° N	64
L03	Sanyangpo landslide	Baqiao, Xi'an	Loess Tableland area	109.11° E	34.25° N	40
L04	Hongfu temple landslide	Chang'an, Xi'an	Loess Tableland area	108.97° E	34.10° N	25
L05	Miaodian landslide	Jingyang, Xianyang	Loess Tableland area	108.81° E	34.50° N	139
L06	Dabuzi landslide	Jingyang, Xianyang	Loess Tableland area	108.86° E	34.48° N	322
L07	Moping landslide	Jingbian, Yulin	Loess Hilly area	108.58° E	37.07° N	114
L08	Qiaocha landslide	Zhidan, Yan'an	Loess Hilly area	108.62° E	36.96° N	67
L09	Songzhuang landslide	Zhidan, Yan'an	Loess Hilly area	108.57° E	36.96° N	59
L10	Hanjiagou landslide	Zhidan, Yan'an	Loess Hilly area	108.49° E	36.67° N	43
L11	Zhifang school landslide	Zhidan, Yan'an	Loess Hilly area	108.61° E	36.84° N	162

Id	Flight altitude (m)	DOM resolution (cm)	DEM resolution (cm)	Overlap (%)	Sidelap (%)	Tilt angle (°)
L01	149.7	5.65	11.3	75	75	− 45
L02	143	4.4	8.8	70	70	− 45
L03	165	5.12	10.24	75	75	− 45
L04	76.5	2.42	4.84	80	80	− 45
L05	93.4	2.9	5.8	75	75	− 45
L06	90	2.82	5.64	75	75	− 45
L07	171	5.24	10.48	75	75	− 45
L08	148	4.62	9.24	75	75	− 45
L09	115.5	3.63	7.26	80	75	− 45
L10	146.4	4.54	9.08	75	75	− 45
L11	107.1	3.37	6.73	75	75	− 45

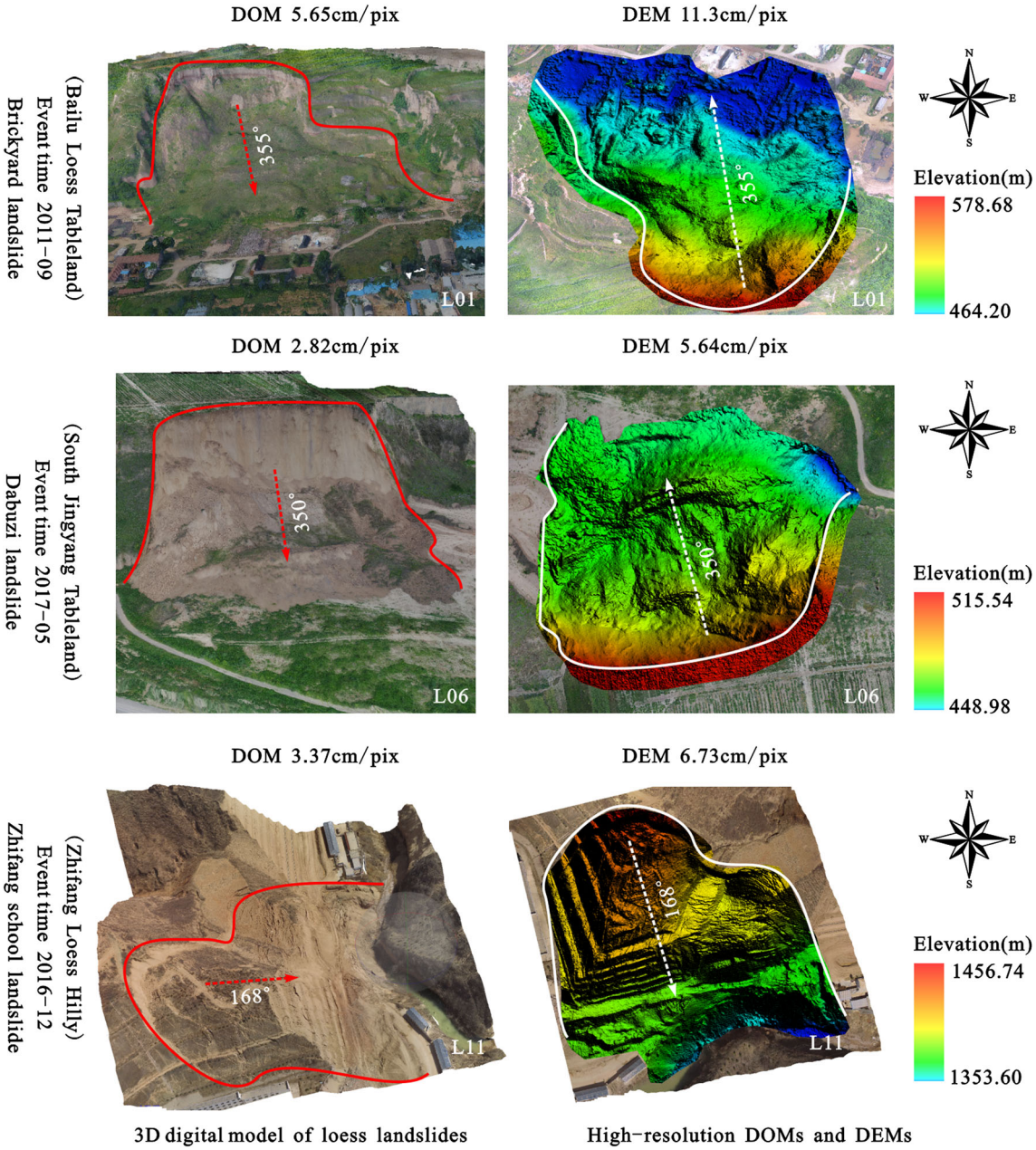

Fig. 8 High-resolution 3D model, DOMs, and DEMs of typical loess landslides based on UAV and SfM techniques

Similarly, three longitudinal cross-sections (AA′, BB′, and CC′) and three transverse cross-sections (DD′, EE′, and FF′) are set on the 2D surface of the L06 landslide. The structural frame of the L06 landslide that can be constructed from these six cross-sections consists mainly of four parts, namely, the top, the main scarp, the main body, and the toe (Fig. 13). The L06 landslide, another homogenous loess landslide, has a conspicuous sliding plane and an arc-shaped main scarp. In addition, the L06 landslide has a maximum difference in elevation of 65.56 m, a horizontal sliding distance of approximately 33 m, and a maximum gradient of nearly 80°. In terms of the South Jingyang Tableland with approximately 45° original slope, because of slope excavation, agricultural irrigation, flurosion, rainfall, and other factors, tableland edge is constantly being eroded and destroyed. Thus, original slope will become more gentle as a whole when the landslide occurred. But locally, slope of the middle and the lower part in landslide is much smaller than original slope and slope of main scarp (nearly 80°) is much steeper than it used to be (flat), as shown in Fig. 1 and Fig. 13. The main body of L06 landslide has a maximum accumulation depth of 19 m. Migoń et al. (2017) considered it as a mechanism which large-scale slope is remodeled by landslides for the sake of their strength equilibrium. Over time, the steep part of landslide top will slide again and again until the gravitational potential energy is all released in this cyclic process. Which is the process and mechanism of loess landslide change the topography of Loess Tableland area, such as the South Jingyang Tableland in Shaanxi

Table 3 Statistics of topography and geometry characteristics in landslides

Id	Average elevation (m)	Average gradient (°)	Average relief (m)	Relative height difference (m)	Length (m)	Width (m)	Thickness (m)	Perimeter (m)
L01	490.07	20.97	1.43	114.47	339.33	315.27	93	1143
L02	498.72	43.23	6.82	85.51	58.75	200.01	33	455.84
L03	510.39	23.54	3.08	66.09	157.66	80.72	25.1	492.92
L04	545.50	35.03	6.01	26.79	26.245	23.01	16	100.54
L05	466.64	30.64	4.53	68.18	119.39	86.10	12.6	387.37
L06	474.48	27.50	3.73	65.56	121.55	133.46	19	501.95
L07	1420.57	38.10	6.30	28.87	23.87	44.62	22	135.68
L08	1327.61	39.84	6.26	42.05	35.98	124.96	23	329.8
L09	1310.32	35.41	4.87	46.88	46.53	43.26	24	193.11
L10	1294.15	41.24	6.49	75.57	68.05	125	54	355.90
L11	1399.04	29.85	4.02	103.14	174.23	172.23	76	650.66

Id	Area (m^2)	Main sliding direction (°)	Length/width ratio (%)	Thickness/length ratio (%)	Plane morphology	Profile morphology
L01	100,900	355	1.08	0.27	Tongue	Concave
L02	6940	132	0.29	0.56	Obtuse triangle	Convex
L03	13,460	47	1.95	0.16	Tongue	Convex
L04	687	30	1.14	0.61	Fan	Mixed
L05	10,640	34	1.39	0.11	Fan	Concave
L06	15,660	350	0.91	0.16	Rectangle	Concave
L07	753	223	0.53	0.92	Semicircle	Linear
L08	3269	151	0.29	0.64	Semi-ellipse	Linear
L09	2135	91	1.08	0.52	Rectangle	Linear
L10	6850	97	0.54	0.79	Acute triangle	Linear
L11	24,080	168	1.01	0.44	Semicircle	Convex

*Relief calculation window size, 5 m × 5 m

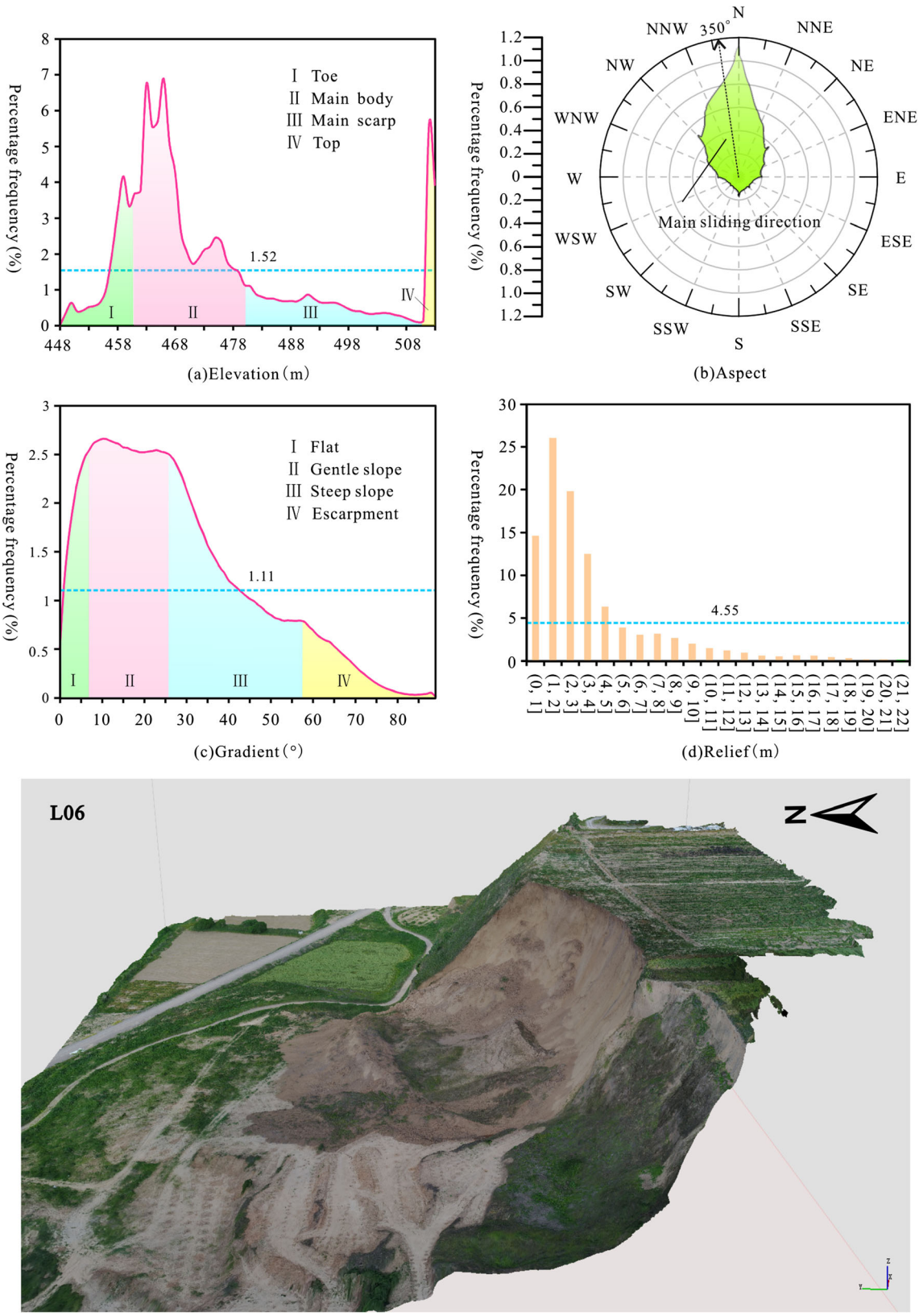

Fig. 9 The percentage frequency distribution of characteristic parameters of the L06 landslide in the South Jingyang Tableland

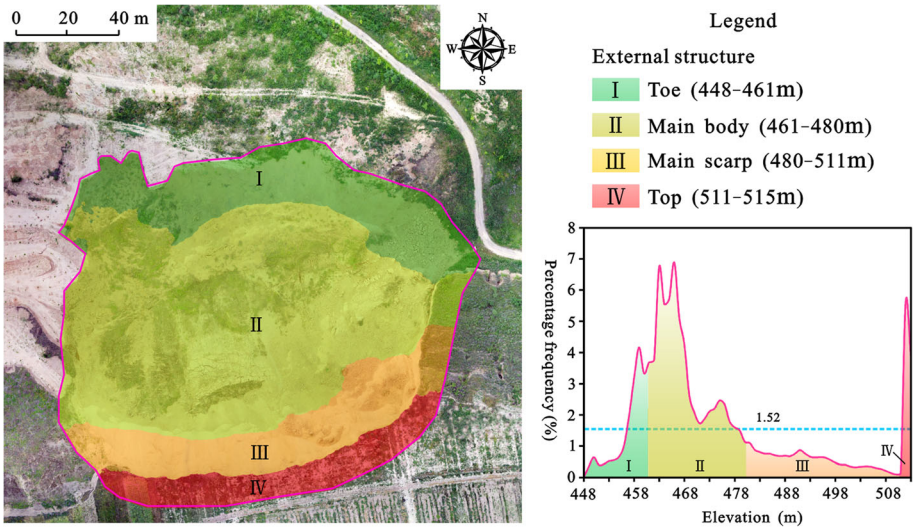

Fig. 10 Identifying the external structure of the L06 landslide according to the elevation frequency curve in Fig. 9a

province (Wang et al. 2017; Leng et al. 2017) and the Heifangtai Tableland in Gansu province (Peng et al. 2017a, b; Zhang and Wang 2017; Qi et al. 2017).

Surface feature analysis

Niethammer et al. (2009, 2012) concluded that high-resolution orthoimages acquired by UAVs could enable us to analyze the surface features of landslides in detail; specifically, they determined the displacement, fissures, and difference in soil moisture of the Super-Sauze landslide by comparing high-resolution images (Niethammer et al. 2009; Niethammer et al. 2012), which clearly showed the length, width, and depth of each fissure (Grandjean et al. 2007; Niethammer et al. 2012). Previous research results have demonstrated that landslide fissures are formed by the same mechanism by which glacier crevasses are formed, and stable bedrock fissures will gradually affect the movement and dynamic process of the whole landslide (Wilhelm 1975; Kääb 2002; Malet et al. 2005). Not only do loess landslides have similar fissures but they also have unique micro-landforms (e.g., loess sinkholes and gully erosion) that are primarily formed due to erosion by flowing water. Therefore, analyzing the surface features of loess landslides may help us to understand some of their dynamic mechanisms. The morphology, structure, outline, spatial location, land use of the surrounding area, and surface texture details of a loess landslide can be clearly seen in the high-resolution orthoimages captured by UAVs (Figs. 14, 15, and 16). For the L11 landslide (as shown in Fig. 14), dozens of tensile fissures have formed in three directions (E-W, NW-SE, NE-SW) as a result of the southward movement of the whole landslide. In the orthoimage of the L11 landslide (Fig. 14), an arc belt-shaped main scarp can be clearly observed, and the newly exposed loess exhibits a bright white color. In addition, landslide deposits have encroached on the water drains, but fortunately, have not completed blocked the river channel. Because of the loose texture of loess and the developed vertical joints, traces of erosion by flowing water can be seen everywhere from the surface to underground in the Lo8 landslide, resulting in microtopography has been gradually formed (Fig. 15). A long loess sinkhole can be seen

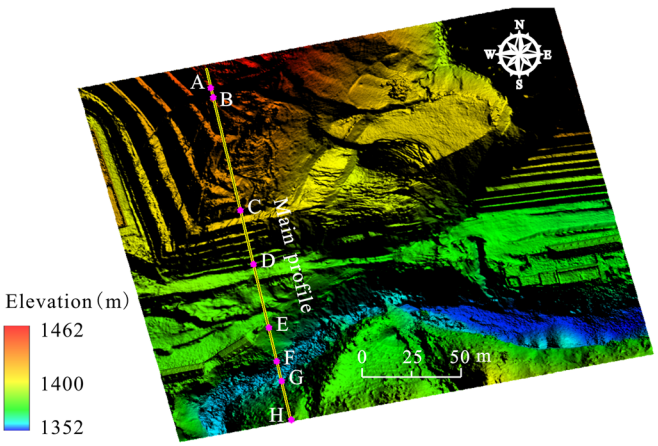

Fig. 11 Main profile position of the L11 landslide in the Loess Hilly area

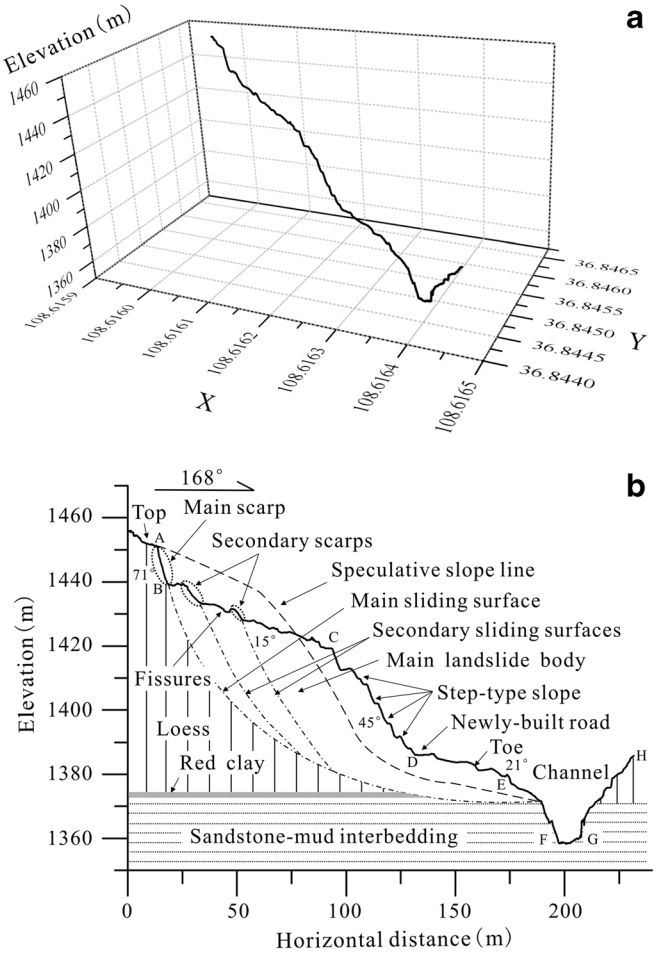

Fig. 12 **a** 3D profile and **b** 2D sectional structure of the L11 landslide

in the high-resolution image of the Lo8 landslide (Fig. 15). The upper part of this loess sinkhole is 13 m in length, and the lower part is a cave with a diameter of 2.4 m. The presence of the loess sinkhole disrupts the stable internal structure of the loess landslide and is very likely to induce a new loess landslide (Fig. 15). Another microtopography is gully erosion. In the high-resolution image of the Lo6 landslide (Fig. 16), three nearly 50-m-long gullies (labeled L1, L2, and L3) that formed due to erosion by flowing water can be seen to the east of the landslide. An analysis of the profile shows that gully L3 is approximately 2.9 m in width and 3.8 m in depth at cross-section AB. Under erosion by flowing water, these gullies, which formed over an extended period of time, will continuously erode into the slope of the South Jingyang Tableland and disrupt its stability. This is very likely a unique mechanism by which this type of landslide is induced. Therefore, we predict that a new landslide will occur in this area and bury the road below in the future.

Hydrology analysis

Hydrological analysis of landslide masses is one of the focuses of geographical research (Malet et al. 2005; Niethammer et al. 2009). In the past, it was very difficult to construct accurate hydrological models due to the limitations of the accuracy of conventional DEMs. Today, the SfM and UAV techniques can produce high-resolution topographic models for landslides, providing technical support for constructing high-accuracy hydrological models of landslides. As previously mentioned, many surface fissures will be formed after a landslide occurs. Rainfall and flowing water continuously alter the microtopography on the surface of a landslide. Therefore, analyzing the hydrological paths on the loess landslide mass is of great importance to the understanding of its surface erosion and landform evolution as well as its stability analysis. Because the L11 landslide is part of a drain catchment area, its hydrological paths were analyzed using the ArcSWAT 2012 hydrological model. Figure 17a shows the spatial distribution of the longest hydrological path on the L11 landslide. Figure 17b–i shows the hydrological paths and sub-catchment areas under various minimum catchment areas. As demonstrated in Figs. 17 and 18, both the number of sub-catchment areas and the total length of the hydrological paths gradually decrease as the catchment area threshold increases. When the threshold is greater than 300 m^2, there is almost no significant difference between the extracted sub-catchment areas and the hydrological paths. Under this threshold, the obtained hydrological paths should be the areas most intensely eroded by flowing water on the landslide mass. Therefore, special attention should be given

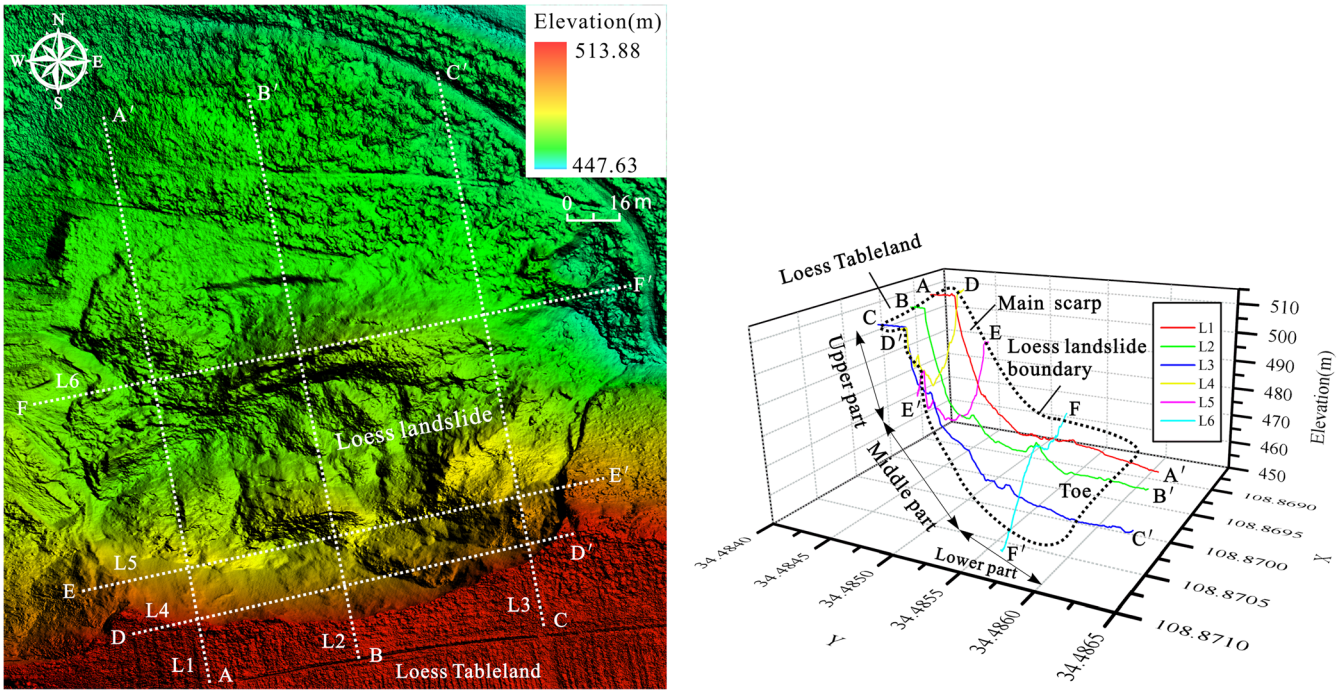

Fig. 13 2D and 3D section frame of the L06 landslide in the South Jingyang Tableland

to monitoring these areas where may be the most heavily eroded and unstable areas.

Discussion

In this study, we used the UAV measuring platform and SfM modeling technique for estimating three-dimensional structures from two-dimensional image sequences that have become relatively popular in recent years to acquire high-resolution surface topographic and image data. We constructed 3D images of some runoff plots on our campus using a low-cost UAV, through which we preliminarily examined its accuracy. A high-resolution DOM (1.56 cm/pix) and a high-resolution DEM (3.11 cm/pix) were obtained by conducting UAV flights, demonstrating that the UAV-acquired data had very high relative accuracy. DOMs and DEMs obtained without adding GCPs had a horizontal repeat error of approximately ± 0.5 m and a vertical repeat error of approximately ± 0.2 m. Our main objective was to perform high-resolution spatial analysis on landslides, which did not involve the monitoring of

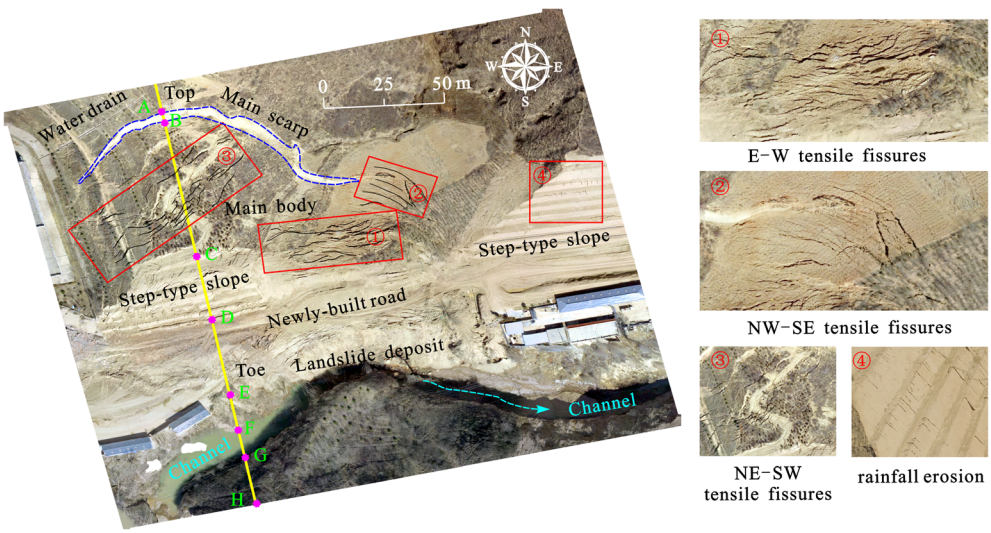

Fig. 14 High-resolution DOM and surface features of the L11 landslide

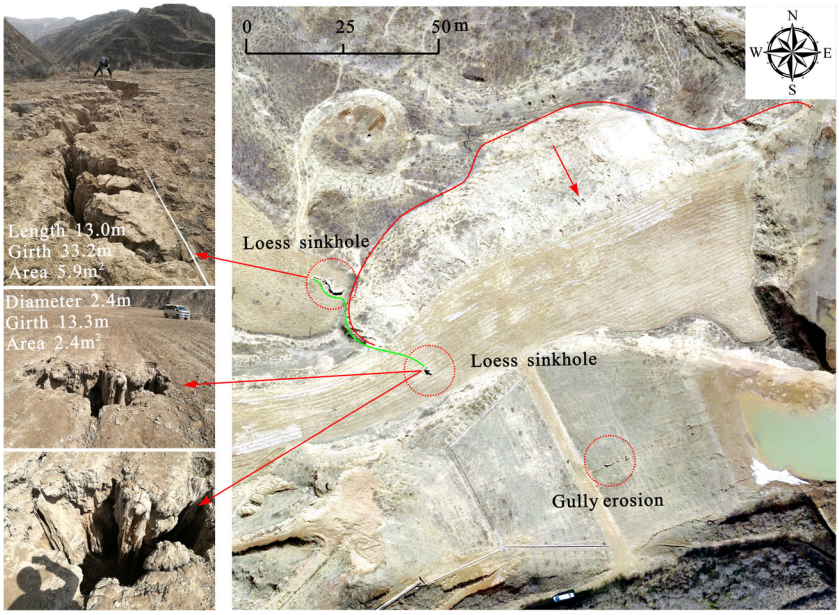

Fig. 15 High-resolution DOM and surface features of the L08 landslide

their displacements. However, for landslide monitoring, GCPs are required to increase data accuracy because the coordinates of GCPs can be used to generate a more accurate model with absolute coordinates (Lucieer et al. 2014; Benoit et al. 2015; Pineux et al. 2017). It is worth mentioning that some advanced drones equipped high-precision GNSS or Inertial Navigation System which can avoid GCP measurements has been introduced into landslide measurement in the past few years (Carrillo et al. 2012; Eure et al. 2013; Lindner et al. 2016). Besides, the GCPs measurements are not only dangerous but time-consuming and so expensive procedures. Nonetheless, this new non-contact measuring technique is low cost, safe, and fast and can generate high-resolution data using UAVs, a modern tool that can easily acquire topographic and landform data. Therefore, an increasing number of geologists and geomorphologists have begun to use UAVs to acquire data (Ruzgienė et al. 2015; Uysal et al. 2015; Kršák et al. 2016; Cook 2017; Dąbski et al. 2017). Moreover, using a combination of UAVs and LiDAR, InSAR, and 3D laser scanners has become a new trend (Cawood et al. 2017; Cook 2017; Gruszczyński et al. 2017).

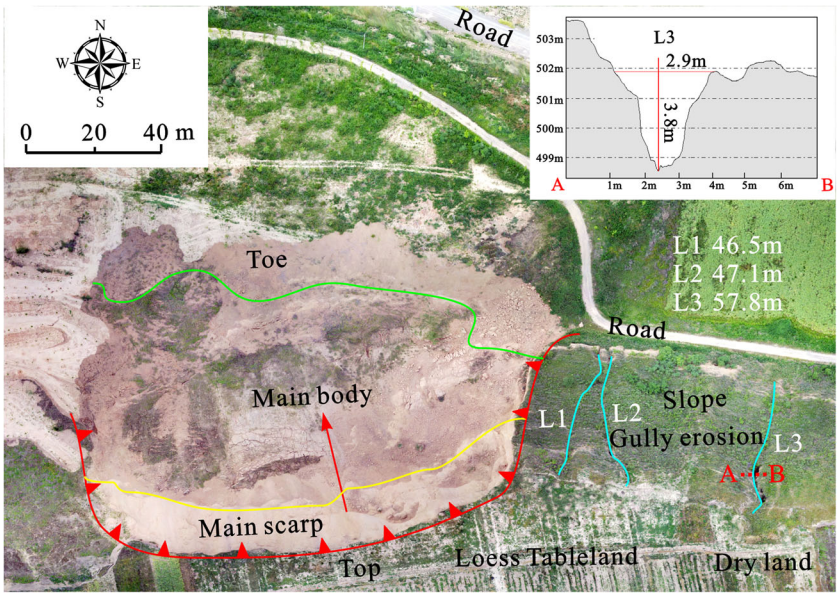

Fig. 16 High-resolution DOM and surface features of the L06 landslide

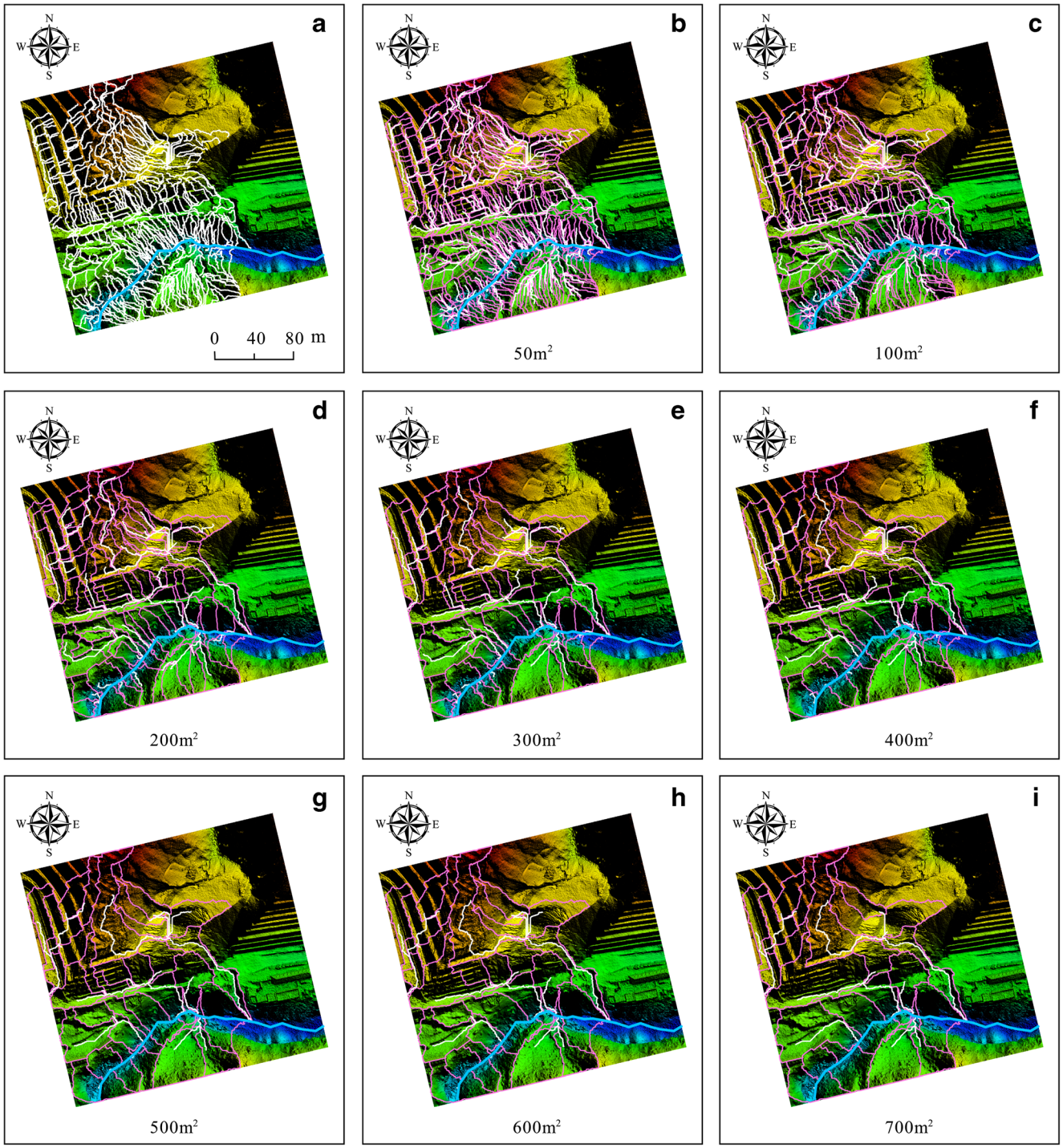

Fig. 17 Hydrological paths and sub-catchments of the L11 landslide under different minimum drainage area thresholds

The UAV photogrammetric technique is very suitable for the Loess Plateau because of the sparse vegetation (low coverage) and large areas of bare rock and soil in this region (Peng et al. 2017a, b). Evidently, some caveats exist for UAV flights in the field. First, local laws and regulations must be followed. UAV flights must not endanger public safety or military secrets (e.g., flights over airports or sensitive military zones). Second, approximately 10~20 flight batteries should be prepared for fieldwork. Flight routes should be reasonably planned based on the topography and altitude of the landslide. Efforts should be made to ensure both relatively high resolution and flight safety. Third, selecting favorable weather conditions is also crucial. UAV flights should be conducted on sunny, no-wind or low-wind days. Finally, experienced UAV flight operators are also necessary (Niethammer et al. 2012).

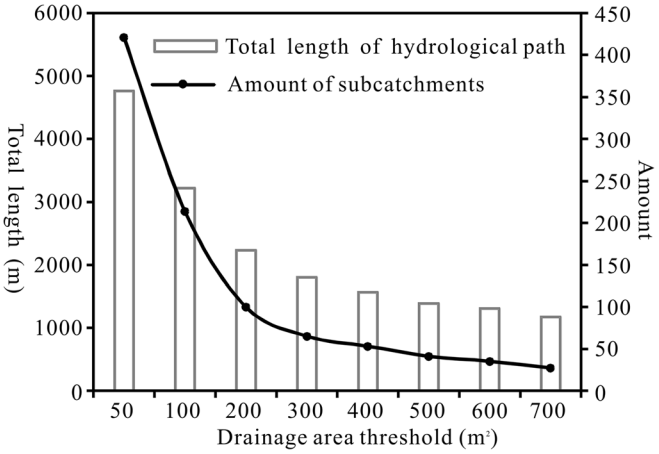

Fig. 18 The length of hydrological paths and number of sub-catchments decrease as the threshold increases

Conclusions

In this paper, we demonstrate the use of low-cost quad-rotor UAVs to acquire high-resolution topographic data and images. Satisfactory results were achieved. Spatial analysis (mainly including geometric feature analysis, topographic profile analysis, surface feature analysis, and hydrological analysis) of loess landslides was then performed using the high-resolution DOMs and DEMs acquired by the UAVs. Using conventional measuring methods to determine the characteristic geometric parameters of landslides is a very complex, time-consuming, and effort-intensive task. Today, the SfM and UAV techniques can simplify this task and significantly improve work efficiency and measuring accuracy. Using 3D and GIS spatial analysis technologies, we obtained the characteristic parameters (e.g., morphological characteristics, elevation distribution, relief, size, circularity, and sliding direction) of 11 loess landslides easily. By statistically analyzing the percentage frequency distributions of elevation, aspect, gradient, and relief of single loess landslide, we reveal that these frequency distribution curves are uniquely advantageous in identifying the structural composition and main sliding direction of each landslide. A combination of 3D profile analysis and proper ground surveys can facilitate accurate determination of the structural characteristics of a landslide in detail (e.g., profile shape, fissures, step-type slope, main scarp, and gradient variation) and can even help us deduce the sliding plane, the original slope shape, and the accumulation depth of a landslide. A high-resolution DOM more clearly manifests the morphology, structure, outline, spatial location, land use in the surrounding area, and surface texture details of a landslide than does a conventional satellite image. Microtopography, such as loess sinkholes and gullies formed due to erosion by flowing water, may induce new loess landslides. The stability of loess slopes is disrupted by erosion by flowing water, and this may be one of the unique mechanisms by which landslides are induced. High-resolution DEMs provide a basis for constructing hydrological models of landslides in catchment areas. For loess landslides that are extremely prone to erosion by rainfall and flowing water, extracting hydrological paths in catchment areas on their surfaces is of great importance to the monitoring of their surface erosion, geomorphological evolution, deformation, and displacement.

Funding information This research was funded by the National Natural Science Foundation of China (Grant No. 41771539), International Partnership Program of Chinese Academy of Sciences (Grant No. 131551KYSB20160002), and the China Postdoctoral Science Foundation (Grant No. 2016M602743).

References

Al-Rawabdeh A, He F, Moussa A, El-Sheimy N, Habib A (2016) Using an unmanned aerial vehicle-based digital imaging system to derive a 3D point cloud for landslide scarp recognition. Remote Sens 8(2):95–126. https://doi.org/10.3390/rs8020095

Bayer B, Simoni A, Schmidt D, Bertello L (2017) Using advanced InSAR techniques to monitor landslide deformations induced by tunneling in the Northern Apennines, Italy. Eng Geol 226:20–32. https://doi.org/10.1016/j.enggeo.2017.03.026

Benoit L, Briole P, Martin O, Thom C, Malet JP, Ulrich P (2015) Monitoring landslide displacements with the Geocube wireless network of low-cost GPS. Eng Geol 195:111–121. https://doi.org/10.1016/j.enggeo.2015.05.020

Carrillo LRG, López AED, Lozano R, Pégard C (2012) Combining stereo vision and inertial navigation system for a quad-rotor UAV. J Intell Robot Syst 65(1–4):373–387. https://doi.org/10.1007/s10846-011-9571-7

Carter WE, Shrestha RL, Slatton KC (2007) Geodetic laser scanning. Phys Today 60(12):41–47. https://doi.org/10.1063/1.2825070

Casagli N, Cigna F, Bianchini S, Hölbling D, Füreder P, Righini G, Del CS, Friedl B, Schneiderbauer S, Iasio C, Vlcko J, Greif V, Proske H, Granica K, Falco S, Lozzi S, Mora O, Arnaud A, Novali F, Bianchi M (2016) Landslide mapping and monitoring by using radar and optical remote sensing: examples from the EC-FP7 project SAFER. Remote Sens Appl Soc Environ 4:92–108. https://doi.org/10.1016/j.rsase.2016.07.001

Cawood AJ, Bond CE, Howell JA, Butler RWH, Totake Y (2017) LiDAR, UAV or compass-clinometer? Accuracy, coverage and the effects on structural models. J Struct Geol 98:67–82. https://doi.org/10.1016/j.jsg.2017.04.004

Chen JX, Wang ZY, Song F, Zhao F (2013) Characteristics and prevention measures of loess landslide hazards. Beijing: Metallurgical Industry Press

Cook KL (2017) An evaluation of the effectiveness of low-cost UAVs and structure from motion for geomorphic change detection. Geomorphology 278:195–208. https://doi.org/10.1016/j.geomorph.2016.11.009

Cui Y-f, Zhou X-j, Guo C-x (2017) Experimental study on the moving characteristics of fine grains in wide grading unconsolidated soil under heavy rainfall. J Mt Sci 14(3):417–431

Daakir M, Pierrot-Deseilligny M, Bosser P, Pichard F, Thom C (2015) UAV onboard photogrammetry and GPS positioning for earthworks. Int Arch Photogramm Remote Sens Spatial Inf Sci XL-3/W3:293–298

Dąbski M, Zmarz A, Pabjanek P, Korczak-Abshire M, Karsznia L, Chwedorzewska K (2017) UAV-based detection and spatial analyses of periglacial landforms on Demay Point (King George Island, South Shetland Islands, Antarctica). Geomorphology 29:29–38
Derbyshire E, Mellors TW (1988) Geological and geotechnical characteristics of some loess and loessic soils from China and Britain: a comparison. Eng Geol 25(2):135–175. https://doi.org/10.1016/0013-7952(88)90024-5
Eure KW, Quach CC, Vazquez SL, Hogge EF, Hill BL (2013) An application of UAV attitude estimation using a low-cost inertial navigation system. **NASA Technical Report** https://ntrs.nasa.gov/search.jsp?R=20140002398
Fernández T, Pérez J, Cardenal J, Gómez J, Colomo C, Delgado J (2016) Analysis of landslide evolution affecting olive groves using UAV and photogrammetric techniques. Remote Sens 8(10):837. https://doi.org/10.3390/rs8100837
Flageollet JC, Malet JP, Maquaire O (2000) The 3D structure of the super-sauze earthflow: a first stage towards modelling its behaviour. Phys Chem Earth Part B 25(9):785–791. https://doi.org/10.1016/S1464-1909(00)00102-7
Flint RF (1947) Glacial geology and the Pleistocene epoch. Q Rev Biol 4(1):113–114
Grandjean G, Malet JP, Bitri A, Méric O (2007) Geophysical data fusion by fuzzy logic for imaging the mechanical behaviour of mudslides. Bull Soc Geol Fr 177(2):127–136
Gruszczyński W, Matwi W, Ćwiąkała P (2017) Comparison of low-altitude UAV photogrammetry with terrestrial laser scanning as data-source methods for terrain covered in low vegetation. ISPRS J Photogramm Remote Sens 126:168–179. https://doi.org/10.1016/j.isprsjprs.2017.02.015
Hsieh YC, Chan Y, Hu J (2016) Digital elevation model differencing and error estimation from multiple sources: a case study from the Meiyuan Shan landslide in Taiwan. Remote Sens 8(3):199. https://doi.org/10.3390/rs8030199
James MR, Robson S, d'Oleire-Oltmanns S, Niethammer U (2017) Optimising UAV topographic surveys processed with structure-from-motion: ground control quality, quantity and bundle adjustment. Geomorphology 280:51–66. https://doi.org/10.1016/j.geomorph.2016.11.021
Kääb A (2002) Monitoring high-mountain terrain deformation from repeated air- and spaceborne optical data: examples using digital aerial imagery and ASTER data. ISPRS J Photogramm Remote Sens 57(1):39–52. https://doi.org/10.1016/S0924-2716(02)00114-4
Kršák B, Blišťan P, Pauliková A, Puškárová P, Kovanič Ľ, Palková J, Zelizňaková V (2016) Use of low-cost UAV photogrammetry to analyze the accuracy of a digital elevation model in a case study. Measurement 91:276–287. https://doi.org/10.1016/j.measurement.2016.05.028
Lei XY (2017) The cause of formation, prevention and cure of geological disasters of loess. Peking University Press, Beijing
Leng YQ, Peng JB, Wang QY, Meng ZJ, Huang WL (2017) A fluidized landslide occurred in the Loess Plateau: a study on loess landslide in South Jingyang tableland. Eng Geol. https://doi.org/10.1016/j.enggeo.2017.05.006
Lindner G, Schraml K, Mansberger R, Hübl J (2016) UAV monitoring and documentation of a large landslide. Appl Geomatics 8(1):1–11. https://doi.org/10.1007/s12518-015-0165-0
Liu TS (1985) Loess and environment. China Ocean Press, Beijing
Liu TS, Chang TH (1962) The Huangtu (loess) of China. Acta Geol Sin 42:1–14
Lucieer A, Jong SM, Turner D (2014) Mapping landslide displacements using structure from motion (SfM) and image correlation of multi-temporal UAV photography. Prog Phys Geogr 38(1):97–116. https://doi.org/10.1177/0309133313515293
Malet JP, Van Asch TWJ, Van BR, Maquaire O (2005) Forecasting the behaviour of complex landslides with a spatially distributed hydrological model. Nat Hazards Earth Syst Sci 5(1):71–85
Metternicht G, Hurni L, Gogu R (2005) Remote sensing of landslides: an analysis of the potential contribution to geo-spatial systems for hazard assessment in mountainous environments. Remote Sens Environ 98(2-3):284–303. https://doi.org/10.1016/j.rse.2005.08.004
Migoń P, Jancewicz K, Różycka M, Duszyński F, Kasprzak M (2017) Large-scale slope remodelling by landslides—geomorphic diversity and geological controls, Kamienne Mts. Central Europe. Geomorphology 289:134–151. https://doi.org/10.1016/j.geomorph.2016.09.037
Niethammer U, James MR, Rothmund S, Travelletti J, Joswig M (2012) UAV-based remote sensing of the Super-Sauze landslide: evaluation and results. Eng Geol 128(11):2–11. https://doi.org/10.1016/j.enggeo.2011.03.012
Niethammer U, Rothmund S, Joswig M (2009) UAV-based remote sensing of the slow-moving landslide Super-Sauze. Proceedings of the International Conference on Landslide Processes: From Geomorpholgic Mapping to Dynamic Modelling, Strasbourg, France
Ouédraogo MM, Degré A, Debouche C, Lisein J (2014) The evaluation of unmanned aerial system-based photogrammetry and terrestrial laser scanning to generate DEMs of agricultural watersheds. Geomorphology 214:339–355. https://doi.org/10.1016/j.geomorph.2014.02.016
Peng DL, Xu Q, Dong XJ, Qi X, Ju YZ, Li HJ (2017a) Accurate and efficient method for loess landslide fine mapping with high resolution close-range photogrammetry. J Eng Geol 25(2):424–435
Peng DL, Xu Q, Liu FZ, He YS, Zhang S, Qi X, Zhao KY, Zhang XL (2017b) Distribution and failure modes of the landslides in Heitai terrace, China. Eng Geol. https://doi.org/10.1016/j.enggeo.2017.09.016
Peng JB, Fan ZJ, Wu D, Zhuang JQ, Dai FC, Chen WW, Zhao C (2015) Heavy rainfall triggered loess–mudstone landslide and subsequent debris flow in Tianshui, China. Eng Geol 186:79–90. https://doi.org/10.1016/j.enggeo.2014.08.015
Peterman V (2015) Landslide activity monitoring with the help of unmanned aerial vehicle. Int. Arch. Photogramm. Remote Sens. Spatial Inf. Sci. XL-1-W4:215–218
Pineux N, Lisein J, Swerts G, Bielders CL, Lejeune P, Colinet G, Degré A (2017) Can DEM time series produced by UAV be used to quantify diffuse erosion in an agricultural watershed? Geomorphology 280:122–136. https://doi.org/10.1016/j.geomorph.2016.12.003
Qi X, Xu Q, Liu FZ (2017) Analysis of retrogressive loess flowslides in Heifangtai, China. Eng Geol. https://doi.org/10.1016/j.enggeo.2017.08.028
Qiu HJ, Cao MM, Liu W (2013) Power-law correlations of landslides: a case of Ningqiang County. Geol Sci Technol Inf 32(3):183–187
Qiu HJ, Cui P, Regmi AD, Wang YM, Hu S (2017) Slope height and slope gradient controls on the loess slide size within different slip surfaces. Phys Geogr 38(4):303–317. https://doi.org/10.1080/02723646.2017.1284581
Qiu HJ, Regmi AD, Cui P, Cao MM, Lee JZ, Zhu XH (2016) Size distribution of loess slides in relation to local slope height within different slope morphologies. Catena 145:155–163. https://doi.org/10.1016/j.catena.2016.06.005
Razak KA, Santangelo M, Westen CJV, Straatsma MW, Jong SMD (2013) Generating an optimal DTM from airborne laser scanning data for landslide mapping in a tropical forest environment. Geomorphology 190(3):112–125. https://doi.org/10.1016/j.geomorph.2013.02.021
Ruzgienė B, Berteška T, Gečyte S, Jakubauskienė E, Aksamitauskas VČ (2015) The surface modelling based on UAV photogrammetry and qualitative estimation. Measurement 73:619–627. https://doi.org/10.1016/j.measurement.2015.04.018
Shafique M, van der MM, Khan MA (2016) A review of the 2005 Kashmir earthquake-induced landslides; from a remote sensing prospective. J Asian Earth Sci 118:68–80. https://doi.org/10.1016/j.jseaes.2016.01.002
Shi JS, LZ W, SR W, Li B, Wang T, Xin P (2016) Analysis of the causes of large-scale loess landslides in Baoji, China. Geomorphology 264:109–117. https://doi.org/10.1016/j.geomorph.2016.04.013
Smalley IJ (1971) "In-situ" theories of loess formation and the significance of the calcium-carbonate content of loess. Earth-Sci Rev 7(2):67–85. https://doi.org/10.1016/0012-8252(71)90082-1
Sona G, Pinto L, Pagliari D, Passoni D, Gini R (2014) Experimental analysis of different software packages for orientation and digital surface modelling from UAV images. Earth Sci Inf 7(2):97–107. https://doi.org/10.1007/s12145-013-0142-2
Su X, Meng XM, Wang SY, Wei WH, Feng L (2017) Statistics of characteristic parameters and evolutionary mechanism of landslides in typical area of Longzhong Loess Plateau: a case study of Tianshui city. Quaternary. Sciences 37(2):319–330
Sun Q, Zhang L, Ding XL, Hu J, Li ZW, Zhu JJ (2015) Slope deformation prior to Zhouqu, China landslide from InSAR time series analysis. Remote Sens Environ 156:45–57. https://doi.org/10.1016/j.rse.2014.09.029
Sun WY, Tian YS, Mu XM, Zhai J, Gao P, Zhao GG (2017) Loess landslide inventory map based on GF-1 satellite imagery. Remote Sens 9(314):1–17
Tarolli P (2014) High-resolution topography for understanding earth surface processes: opportunities and challenges. Geomorphology 216:295–312. https://doi.org/10.1016/j.geomorph.2014.03.008
Tofani V, Hong Y, Singhroy V (2014) Introduction: remote sensing techniques for landslide mapping and monitoring. In: Sassa K, Canuti P, Yin YP (eds) Landslide science for a Safer Geoenvironment, vol 2. Springer International Publishing, Cham, pp. 301–303. https://doi.org/10.1007/978-3-319-05050-8_47
Travelletti J, Malet JP (2012) Characterization of the 3D geometry of flow-like landslides: a methodology based on the integration of heterogeneous multi-source data. Eng Geol 128(6):30–48. https://doi.org/10.1016/j.enggeo.2011.05.003
Tu XB, Kwong AKL, Dai FC, Tham LG, Min H (2009) Field monitoring of rainfall infiltration in a loess slope and analysis of failure mechanism of rainfall-induced landslides. Eng Geol 105(1–2):134–150
Turner IL, Harley MD, Drummond CD (2016) UAVs for coastal surveying. Coast Eng 114:19–24. https://doi.org/10.1016/j.coastaleng.2016.03.011
Uysal M, Toprak AS, Polat N (2015) DEM generation with UAV photogrammetry and accuracy analysis in Sahitler hill. Measurement 73:539–543. https://doi.org/10.1016/j.measurement.2015.06.010

Ventisette CD, Righini G, Moretti S, Casagli N (2014) Multitemporal landslides inventory map updating using spaceborne SAR analysis. Int J Appl Earth Obs Geoinformation 30(1):238–246. https://doi.org/10.1016/j.jag.2014.02.008

Wang W, Wang Y, Sun QM, Zhang M, Qiang YX, Liu MM (2017) Spatial variation of saturated hydraulic conductivity of a loess slope in the South Jingyang Plateau, China. Eng Geol. https://doi.org/10.1016/j.enggeo.2017.08.002

Watanabe Y, Kawahara Y (2016) UAV photogrammetry for monitoring changes in river topography and vegetation. Procedia Eng 154:317–325. https://doi.org/10.1016/j.proeng.2016.07.482

Wilhelm F (1975) Schnee- und Gletscherkunde. Walter de Gruyter Press, Berlin

Yang WT, Qi WW, Wang M, Zhang JJ, Zhang Y (2017) Spatial and temporal analyses of post-seismic landslide changes near the epicentre of the Wenchuan earthquake. Geomorphology 276:8–15. https://doi.org/10.1016/j.geomorph.2016.10.010

Zhang DX, Wang GH, Luo CY, Chen J, Zhou YX (2009) A rapid loess flowslide triggered by irrigation in China. Landslides 6(1):55–60. https://doi.org/10.1007/s10346-008-0135-2

Zhang FY, Wang GH (2017) Effect of irrigation-induced densification on the post-failure behavior of loess flowslides occurring on the Heifangtai area, Gansu, China. Eng Geol. https://doi.org/10.1016/j.enggeo.2017.07.010

Zhang ZL, Wang T, Wu S, Tang H, Liang C (2017) Seismic performance of loess-mudstone slope in Tianshui—centrifuge model tests and numerical analysis. Eng Geol 222:225–235. https://doi.org/10.1016/j.enggeo.2017.04.006

Zhuang JQ, Peng JB (2014) A coupled slope cutting—a prolonged rainfall-induced loess landslide: a 17 October 2011 case study. Bull Eng Geol Environ 73(4):997–1011. https://doi.org/10.1007/s10064-014-0645-1

Zhuang JQ, Peng JB, Wang GH, Javed I, Wang Y, Li W (2017) Distribution and characteristics of landslide in Loess Plateau: a case study in Shaanxi province. Eng Geol. https://doi.org/10.1016/j.enggeo.2017.03.00

S. Hu · H. Qiu · N. Wang · J. Wu · D. Yang · M. Cao
College of Urban and Environmental Science,
Northwest University,
Xi'an, 710127, China

S. Hu · H. Qiu · N. Wang · J. Wu · D. Yang
Institute of Earth Surface System and Hazards,
Northwest University,
Xi'an, 710127, China

S. Hu · H. Qiu (✉) · N. Wang · J. Wu · D. Yang
Shaanxi Key Laboratory of Earth Surface System and Environmental Carrying Capacity,
Northwest University,
Xi'an, 710127, China
Email: 13991345616@163.com

X. Wang
State Key Laboratory of Continental Dynamics, Department of Geology,
Northwest University,
Xi'an, 710069, China

Y. Gao
Shaanxi Provincial Land Engineering Construction Group,
Xi'an, 710175, China